Aerodynamic Interference and Performance Changes in "2-lead" Multi-lift System with Helicopters

*DING Zhiwei, DUAN Dengyan, ZHAO Gang, XUAN Jinting, LI Jianbo**

National Key Laboratory of Helicopter Aeromechanics, College of Aerospace Engineering, Nanjing University of Aeronautics and Astronautics, Nanjing 210016, P. R. China

(Received 20 June 2022; revised 15 November 2022; accepted 21 June 2023)

Abstract: As the helicopters in a multi-lift system fly in a close formation, there is severe aerodynamic interference between the wake of the rotors, bringing complex aeromechanics coupling. So it is necessary to investigate interference and resulting performance changes before studying performance optimization and advanced formation control. A baseline configuration of four tandem helicopters carrying a load cooperatively in a "2-lead" formation is performed to explore the interference and performance. A vortex-panel approach based on the viscous vortex particle method is employed to investigate the performances and flow fields in a steady-flight state. The steady-flight state is obtained by a hierarchical trimming method, and the vortex-panel approach is validated by wind tunnel experiments. On this basis, aerodynamic interferences and performances at different flight speeds and variant relative positions are investigated. Computational results indicate that for the baseline configuration, there exists serious interference between helicopters in the front-and-rear arrangement, especially at forward flight. At the advance ratio of 0.1, there exists a 20% thrust loss and a 15% power increase for the front rotor of the tandem helicopter behind the formation. The aerodynamic interference will be reduced significantly if the distance between the front and the rear helicopter meets any of the three conditions below: more than $3.5D$ (D represents the rotor diameter) in the longitudinal direction, more than $0.75D$ in the lateral direction, or more than $0.5D$ in the vertical direction.

Key words: multi-lift; helicopter; performance change; aerodynamic interference; vortex-based approach; formation

CLC number: V211 **Document code:** A **Article ID:** 1005-1120(2023)04-0401-19

0 Introduction

The capability of heavy cargo transportation makes helicopters unique and invaluable in both civil and military applications, especially in situations where other aircrafts cannot easily reach the specified destinations due to operational limits[1-3]. However, the maximum load capacity of a single rotorcraft is usually limited by either excessive power consumption or structural strength. To meet the demand of carrying heavier and heavier loads, the only alternative is using multiple helicopters[4-6].

The concept of using two or more helicopters to carry a load cooperatively, known as the multi-lift system, has been proposed for several decades. Two basic configurations named pendant and spreader bar (shown in Fig.1) respectively have been widely studied. Related research mainly concentrated on dynamics analyses of the coupled system, stability comparison of different load configurations, and control design to improve performance as well as make safe separation[1-3, 6-23]. Although there have been relatively in-depth studies[24] on the interference between aerodynamic components of helicopters, there are few studies on the aerodynamic interference between helicopters in formations with external loads. Ref.[7] proposed a method to simulate disturbances between helicopters and the load by introducing the rotor downwash effect on the

*Corresponding author, E-mail address: ljb101@nuaa.edu.cn.

How to cite this article: DING Zhiwei, DUAN Dengyan, ZHAO Gang, et al. Aerodynamic interference and performance changes in "2-lead" multi-lift system with helicopters[J]. Transactions of Nanjing University of Aeronautics and Astronautics, 2023, 40(4): 401-419.

http://dx.doi.org/10.16356/j.1005-1120.2023.04.003

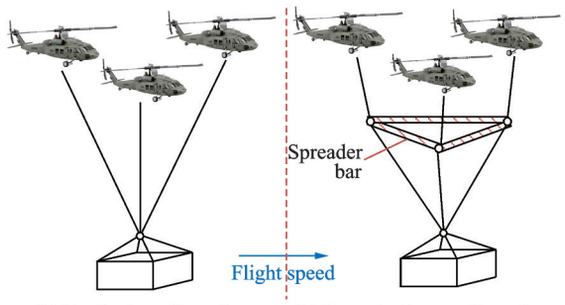

Fig.1 Two basic configurations

load. Wind tunnel tests were conducted to investigate dual lift trim, maneuvers, stability and control in Ref.[8], but only cable aerodynamics and different load attachment techniques were investigated.

Separation distances of two to four rotor diameters are expected to ensure safety for a close formation flight of manned helicopters. The multi-lift system is a typical proximity flight demonstration. Modeling and control analyses for twin-lift system were conducted in Refs.[9-13] and a spreader bar of two rotor diameters long was utilized to guarantee safe helicopter separation. A tighter twin-lift formation with a separation of 1.5 rotor diameters was applied to several civil operations to carry long rigid loads[14]. Ref.[15] proposed a hierarchical controller to carry a slung load by four K-MAX helicopters cooperatively while a separation constraint of 2.26 rotor diameters was imposed in the approach. An experiment was conducted to evaluate stability, control, and simulation of a dual lift system using autonomous helicopters and the results indicated that a two-rotor diameter separation is an optimal compromise between safety and performance[16]. Formation control based on a dynamic inversion controller[17] and performance optimization considering load distribution[18] were performed by Enciu for a multi-lift system of four utility helicopters (similar to UH-60) jointly carrying a 20 000 lb cargo container. In these studies, a separation distance of 100 ft (about 1.9 rotor diameters) was utilized.

Related studies have shown that there exist complex and serious aerodynamic interferences in a proximity flight of rotorcrafts. Ref.[25] describes a study focused on examining the aerodynamic interactions that occur between two helicopters during forward flight. It concluded that there's a significant drop in thrust level for the rotor of the rear helicopter at high flight speeds while in inline arrangement shown in Fig. 2(a) and for the arrangements in Figs.2(b,c) the thrusts are reduced slightly. Similar conclusions were obtained in Ref.[26] and it pointed out that aerodynamic benefits could be achieved by proper formation during rotorcraft proximity flight. Besides, aerodynamic disturbances have been learned systematically[27] and applied to formation control[28] for close flight of multirotors. Some studies related to tiltrotors[29-30] also indicated that close formation flight creates serious aerodynamic interactions. Therefore, as a close formation flight, the aerodynamic interference of the multi-lift system should be explored before high-fidelity modeling and control design.

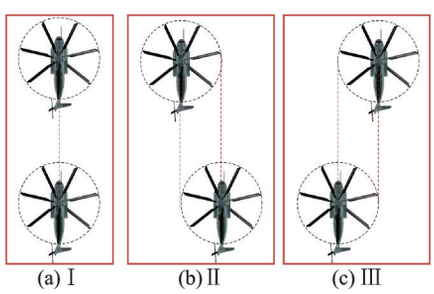

Fig.2 Different arrangements for two helicopters

Moreover, latest research focused more on load distribution for the multi-lift system. The load distribution concept of equalizing cable tension to improve system performance for dual lift system was accepted in most studies[19-23]. It is relatively reasonable for dual lift in side by side arrangement due to the similar characteristics of the two helicopters. For dual lift inline or multi-lift arrangement the equal load distribution strategy seems improper because of load drag which results in backward forces for the front helicopters and forward forces for the rear ones at higher flight speeds. This fact causes that the power consumptions of the front helicopters are greater than the rear helicopters even on equal load distribution. The performance optimization strategy aiming to minimize the maximum helicop-

ter power proposed in Ref.[18] becomes more persuasive. But the power consumption in this paper was calculated by linear interpolation rather than exact trim solution. Besides, aerodynamic interference resulted performance changes were not considered.

The aerodynamic interference between helicopters is investigated in this paper for the multi-lift system. Section 1 presents the baseline configuration of four tandem helicopters carrying a load cooperatively. The aerodynamic interference computation method based on the vortex method is introduced in Section 2. The validation for the computation method is demonstrated in Section 3. On the basis of Section 4, the aerodynamic interference between helicopters at a certain forward speed is calculated and a recommended formation is proposed. At last, Section 5 summarizes the conclusions.

1 Baseline Configuration

The baseline configuration of the multi-lift system consists of four small tandem helicopters and a slung load with a mass of 10 kg. It forms a "2-lead" formation as shown in Fig.3. Each helicopter is connected with the slung load through a four-meters-long cable. The shape of the slung load is a cuboid with length, width, and height of 1, 0.5, and 0.5 m, respectively. And in Fig.3, $x_e y_e z_e$ represents the north-east-down earth coordinate and $x_{ib} y_{ib} z_{ib}$ the body coordinate of the ith helicopter, where x_{ib} points forward, z_{ib} points down and then y_{ib} can be obtained by the right-hand principle. The Euler angles ϕ_i, θ_i, ψ_i between the body and earth axis meets the 3-2-1 rotation principle. The definitions of load's body axis $x_L y_L z_L$ and Euler angles ϕ_L, θ_L, ψ_L are similar to those of helicopters. In addition, XYZ represents the wind-tunnel axis.

Moreover, the configuration of the small tandem helicopter is summarized in Table 1. Each helicopter in the system has a maximum payload capacity of 3.5 kg. As a result, a load mass 10 kg is too heavy to be carried by a single helicopter but can be accommodated by the multi-lift system.

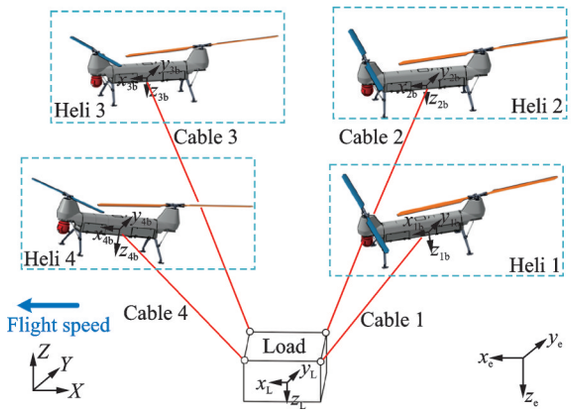

Fig.3 Baseline of the multi-lift system with helicopters

Table 1 Configuration of the tandem helicopter

Item	Value
Takeoff mass / kg	15.0
Inertia on x-axis / (kg·m^2)	0.284
Inertia on y-axis / (kg·m^2)	2.065
Inertia on z-axis / (kg·m^2)	2.083
Radius of rotor / m	0.9
Chord of rotor / m	0.069
Twist angle of rotor / (°)	0
Blade number	2
Rotational speed of rotor / (rad·s^{-1})	113.1
Position of front rotor in body axis / m	(0.582 5, 0, −0.25)
Position of rear rotor in body axis / m	(−0.582 5, 0, −0.25)
Position of suspend point in body axis / m	(0,0,0)

2 Computational Method

2.1 Viscous vortex particle method

Viscous vortex particle method (VVPM) in Refs.[31, 32] is a meshless method adopting Lagrangian description, which can simulate the evolution of rotor wake flow field. Some related studies[30, 33] show that the method can achieve middle to high fidelity apt for rotor aerodynamic research while offering a more efficient calculation process than the classical RANS or LES approach[34]. The discretized vorticity field of VVPM can be expressed as

$$\boldsymbol{\omega}^h(\boldsymbol{r},t)=\sum_{p=1}^{N_p}\boldsymbol{\alpha}_p(t)\,\zeta\big(\boldsymbol{r}-\boldsymbol{r}_p(t);R_p\big) \tag{1}$$

where $\boldsymbol{r}_p(t)$, $\boldsymbol{\alpha}_p(t)$ and R_p are the spatial position,

vorticity density vector and radius of the pth vortex particle, respectively. $\varsigma(\boldsymbol{r})=2e^{-(|\boldsymbol{r}|/\sigma)^2/2}/(2\pi)^{3/2}$ is the cutoff function considering the distribution of vorticity caused by the induction influence of each particle, where σ is the smoothing parameter.

Then consider the vortex dynamics equation (curl form of Navier-Stokes equation) as

$$\frac{D\boldsymbol{\omega}}{Dt}=\boldsymbol{\omega}\cdot\nabla\boldsymbol{u}+\nu\nabla^2\boldsymbol{\omega} \tag{2}$$

where $\boldsymbol{\omega}=\nabla\times\boldsymbol{u}$ is the vorticity field, $D(\cdot)/\mathrm{d}t=\partial(\cdot)/\partial+\boldsymbol{u}(\cdot)$ the material derivative, and $\nabla^2=\partial^2/\partial x^2+\partial^2/\partial y^2+\partial^2/\partial z^2$ the Laplacian operator. The governing equations of vortex particle density and position can be obtained by solving the joint Eq.(1) and Eq.(2), i.e.

$$\begin{cases}\dfrac{\mathrm{d}\boldsymbol{r}_p}{\mathrm{d}t}=\boldsymbol{u}\big(\boldsymbol{r}_p(t),t\big)\\[2ex]\dfrac{\mathrm{d}\boldsymbol{\alpha}_p}{\mathrm{d}t}=\boldsymbol{\alpha}_p\cdot\nabla\boldsymbol{u}\big(\boldsymbol{r}_p(t),t\big)+\nu\big[\nabla^2\boldsymbol{\alpha}_p\big]\end{cases} \tag{3}$$

where $\nu\big[\nabla^2\boldsymbol{\alpha}_p\big]$ is the viscous diffusion effect of vortex particles, which represents the influence of air viscosity in the whole process of vorticity transport.

The equation above is the discrete governing equation in the convection-diffusion form, with the vorticity and spatial position of vortex particles changing with time. The local velocity $\boldsymbol{u}(\boldsymbol{r},t)=\boldsymbol{u}_\infty(\boldsymbol{r},t)+\boldsymbol{u}_i(\boldsymbol{r},t)$ of vortex particles is determined by the combination of free-stream velocity and induced velocity of vorticity field. Here, the induced velocity term can be solved by the Biot-Savart's theorem, i.e.

$$\boldsymbol{u}_i(\boldsymbol{r},t)=\int_{V_0}\boldsymbol{K}(\boldsymbol{r},\boldsymbol{r}_0)\times\boldsymbol{\omega}(\boldsymbol{r}_0,t)\,\mathrm{d}V_0 \tag{4}$$

where $\boldsymbol{K}(\boldsymbol{r},\boldsymbol{r}_0)=G(\boldsymbol{r},\boldsymbol{r}_0)-\varsigma(\boldsymbol{r},\boldsymbol{r}_0)$ is the Biot-Savart kernel, and $G(\boldsymbol{r},\boldsymbol{r}_0)$ the vector form of Green's function. By substituting the governing equation of vortex particle field into the above equation, the solution formula of induced velocity generated by vortex particle field can be obtained as

$$\boldsymbol{u}_i^h(\boldsymbol{r},t)=\sum_{p=1}^{N_p}\boldsymbol{K}^h\big(\boldsymbol{r}-\boldsymbol{r}_p(t)\big)\times\boldsymbol{\alpha}_p(t) \tag{5}$$

The expression of the kernel function should correspond with cutoff function $\varsigma(\boldsymbol{r})$, and the kernel function is the Rosenhead-Moore kernel, where R_v is the radius of the vortex core, which is determined by the resolution of the vortex particles filed as

$$\boldsymbol{K}^h(\boldsymbol{x},\boldsymbol{y})=-\frac{1}{4\pi}\frac{\boldsymbol{x}-\boldsymbol{y}}{\Big(\big|\boldsymbol{x}-\boldsymbol{y}\big|^2+R_v^2\Big)^{3/2}} \tag{6}$$

In this study, $\nu\big[\nabla^2\boldsymbol{\alpha}_p\big]$ is solved by particle strength exchange (PSE) method[35]. The key of PSE method is to replace the Laplacian operator ∇^2 by the integral operator, so as to avoid direct numerical integration. After applying the PSE method, the viscous diffusion term can be written as

$$\left.\frac{\mathrm{d}\boldsymbol{\alpha}_p}{\mathrm{d}t}\right|_{\mathrm{PSE}}=\nu\sum_{j\in P_i}\big(V_p\boldsymbol{\alpha}_p-V_j\boldsymbol{\alpha}_j\big)\varsigma\big(\boldsymbol{x}_p-\boldsymbol{x}_j;R_j\big) \tag{7}$$

where V_p and V_j are the pth and jth particles' volume, respectively. Since the kernel function will decay rapidly with the increase of distance, only the vortex particles close to pth particle will be considered, and the influence of all particles exceeding the set truncation distance will be ignored. Therefore, only the influence of P_i adjacent particles will be reflected in the calculation. In this study, the cutoff distance of PSE method is consistent with the region division distance of acceleration algorithm discussed below.

It can be found from the above induced velocity calculation of vortex particles that the total contribution of N particles needs to be included in the solution of particle convection velocity term or velocity gradient term. This is similar to the classical N-body problem. For this type of problem, TreeCode[36] and fast multipole algorithm (FMM)[37] are two common acceleration algorithms. Both algorithms need to generate corresponding data structures, which are generally in the form of Oct-Tree. If the accelerated algorithm is not adopted, the direct numerical solution scale of N particles is $O(N^2)$. After adopting the accelerated algorithm, the solution scale of TreeCode is $O\big(N\lg N\big)$, and the solution scale of FMM algorithm is $O(N)$. As the time steps increase, the number of vortex particles in the simulation grows rapidly. This highlights the importance of acceleration techniques such as TreeCode and FMM.

Because the interference between multiple rotors is involved, the order of magnitude of vortex particles involved in this study is large. To optimize computational efficiency to the greatest extent possible, the FMM algorithm is used as the acceleration technology. In FMM algorithm, if the interval between two vortex element regions (a divided group of vortex particles) is greater than the set truncation distance, the influence of the source region on the target region is first expanded into a multipole series. In the target region, the multipole series is transformed into a local Taylor expansion, so as the induced velocities of all vortex particles in the region can be quickly gained. FMM algorithm is used to calculate the induced velocities, velocity gradients and viscous diffusion effects of vortex particles.

2.2 Lifting surface/vortex lattice method

The aerodynamic model of rotor blade involves the calculation of rotor thrust, blade flapping and induced velocity. The method of lifting line[38] and lifting surface[39] has been widely used in previous studies. In contrast, the latter has higher calculation accuracy and can analyze more complex blade three-dimensional shapes (such as taper and sweepback). Based on this consideration, the lifting surface/vortex lattice method is used as the blade aerodynamic model.

In the study, the whole blade is divided into several micro segments along the spanwise direction first, then it is represented by the middle arc surface without thickness. For the blade with sweepback and taper, the corresponding mesh lines should be modified at the front and rear edges of the blade, and the grid partition should be corresponding to the blade segments. Fig.4 is a typical case, the lifting surface grid of the blade is divided into S1 and S2 segments, in which the former is a straight-line segment and the latter is a sweepback segment (or taper segment).

As the blade is divided into several parallel columns along the spanwise direction and several rows along the chord direction, the blade surface is composed of many spanwise and chord grids. Although the spanwise number of each blade segment is different, the chord grid number should remain the same. The middle arc surface of the blade is replaced by the vortex quadrilateral, the spanwise attached vortex of the vortex quadrilateral is located at the quarter chord line of the grid, and the chord attached vortex is along the spanwise grid. At the boundary of the grid, the trailing edge vortex of the vortex quadrilateral is located at the quarter chord of the adjacent grid in the chord direction. In the trailing edge area of the blade, the vortex lattice equivalently generates vortex particle clusters, as shown in Fig.5.

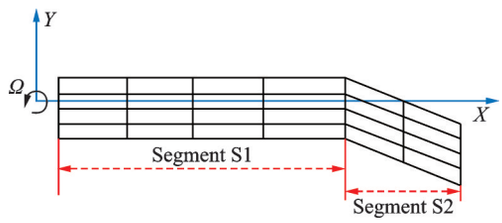

Fig.4 Vortex panel grid partition of a blade with sweepback

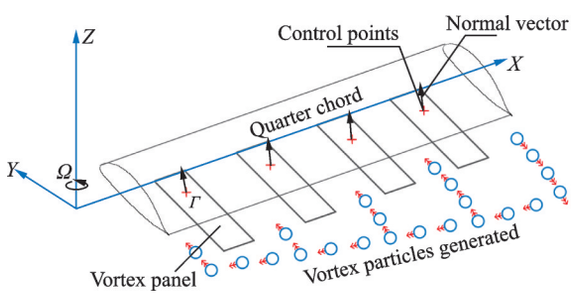

Fig.5 Lifting surface vortex panel distribution and vortex particles generated in trailing edge

The vorticity source generated at each trailing edge of blade segment and shed into rotor wake can be calculated by

$$r_{\text{wake}} = -\frac{\mathrm{d}\boldsymbol{\Gamma}_{\text{b}}}{\mathrm{d}t} + \boldsymbol{v}_{\text{b}} \nabla \cdot \boldsymbol{\Gamma}_{\text{b}} \tag{8}$$

where r_{wake} is the strength of the newly generated vortex, $\boldsymbol{\Gamma}_{\text{b}}$ the vector form of the blade bound circulation, and $\boldsymbol{v}_{\text{b}}$ the local velocity vector of the bound vortex consist of the blade structure (including rotation and flapping) motion, free-stream wind, induced velocity and the interference velocities from other sources. In Eq.(8), the first term on the right-hand side represents the trailing vortex generated by the spanwise change of bound circulation. The second term represents the shed vorticity generated by

the azimuth change of the bound circulation. Consider the panels on the blade in Fig.5 to simulate the shed and trailing vorticity, align particles with the moving trailing edge and emit particles between every two adjacent panels. In the time step, line vortices at the trailing edge ensure zero net vorticity. Additionally, newly generated particles are subject to the Kutta condition at each time step, which helps to maintain vorticity balance at the trailing edge.

2.3 Trimming method

The hybrid hierarchical optimization trimming method from Ref.[40] is used to trim the multi-lift system at different flight speeds, as shown in Fig.6.

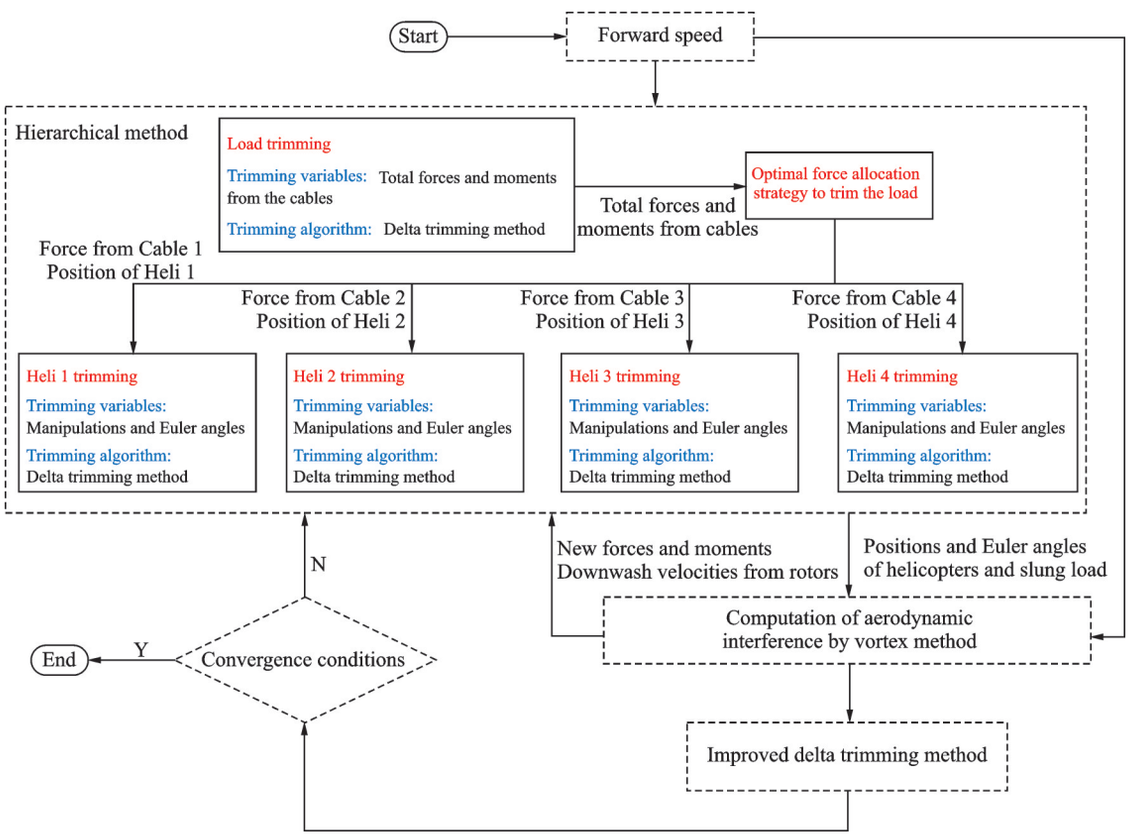

Fig.6 Hybrid hierarchical optimization trimming method in Ref.[40]

The trimming method at a certain flight speed mainly includes the following steps:

Step 1 Load trim. Calculate total forces and moments from cables to trim the load.

Step 2 Using the total forces and moments, apply the optimal force allocation strategy to determine the force distribution among each cable.

Step 3 Trim the four tandem helicopters, and get related trimming variables.

Step 4 Based on the trimming variables, calculate aerodynamic interference by vortex method at the certain flight speed.

Step 5 Introduce the aerodynamic interference into the helicopter and load models.

Step 6 Retrim the load and the helicopter by improved delta trimming method, and get the new trimming variables.

Step 7 If the difference between the last two trimming results is small enough, end trimming; if not, return to Step 4.

It should be noted that the above-mentioned optimal force allocation strategy and trimming results can be found in Ref.[40] in detail.

3 Validation

To validate the computational method, the calculated thrust coefficient and sectional lift coefficients of the Caradonna-Tung rotor in hover, downwash velocities of the scaled model rotor in forward flight, thrust and power coefficients of tandem ro-

tors are predicted and compared with the wind-tunnel test data.

3.1 Caradonna-Tung rotor in hover

The experiment for Caradonna-Tung rotor in hover was conducted in the Army Aeromechanics Laboratory's hover test facility[41]. The two-blade rotor uses NACA0012 airfoil and is untwisted and untapered. The rotor radius and the chord are 1.143 m and 0.19 m, respectively. The cases with collective pitches of 5° and 8°, rotating at 1 250 rad/m are chosen for validation.

Figs.7(a—c) show the velocity magnitude, the wake structure and the tip vortex position for Caradonna-Tung rotor in hover with collective pitch angle θ_c of 8° after 10 rotor revolutions. The tip vortex and bundle region far below the rotor plane are well-captured, showing the contraction, expansion, aperiodic, diffusing and stretching movements of the wake concretely. For the case with collective pitch of 5°, the experimented thrust coefficient C_T is 0.002 4. And for that of 8°, C_T is 0.004 6. As we can see from Fig.7(d), after five revolutions, there is almost no fluctuations of C_T both for the two cases. Furthermore, the errors between the final convergence and the experimental results are less than 5%. Fig.7(e) shows the loading distribution along the radial station. The whole tendencies of the calculation and experimental results are consistent, but there are slight variations in the inboard and outboard regions. In the rotor blade's numerical model, the blade's root was cut-off, so the root vortex is stronger than the experiment blade with an entire blade root. This makes the calculation results of the inboard region lower than the experiment. In the out-

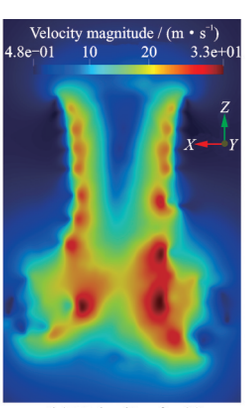

(a) Velocity, θ_c=8°

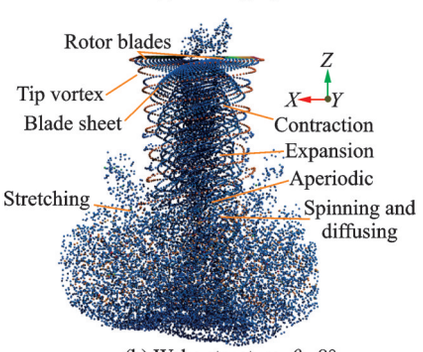

(b) Wake structure, θ_c=8°

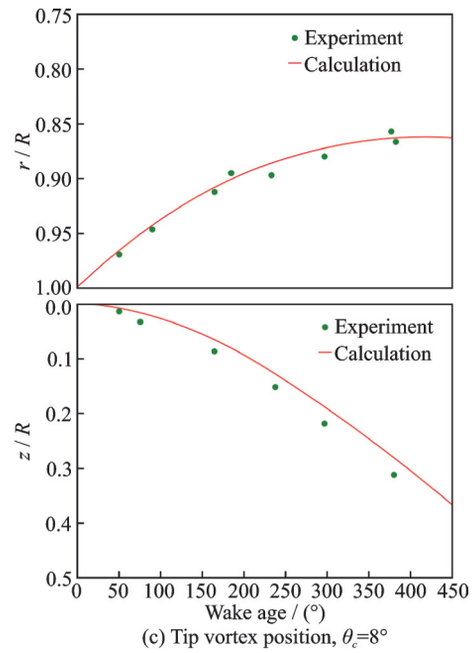

(c) Tip vortex position, θ_c=8°

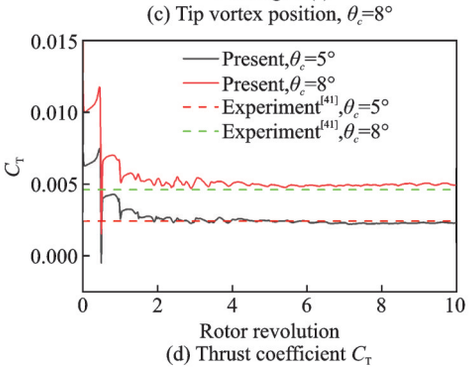

(d) Thrust coefficient C_T

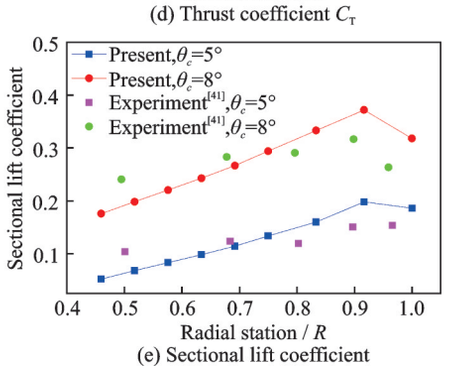

(e) Sectional lift coefficient

Fig.7 Calculation results for the Caradonna-Tung rotor in hover

board region, where flow is transonic, lift capture depends on the Mach number correction model applied to the lift coefficient calculation, which makes the difference between the calculation and experimental results. Similar results could be found in Ref.[42].

3.2 Scaled model rotor in forward flight

The scaled model rotor in the wind-tunnel test[43] has four blades with NACA0012 profile. The rotational speed, rotor radius, chord and linear twist are 2 113 rad/m, 0.861 m, 0.066 m, and −8°, respectively. The constant, cosine and sine terms of blade collective pitch in Fourier series are 6.3°, −2.1° and 2.0°, respectively. The angle between the rotor disk and freestream velocity (positive nose up) is 3°. The flight speed for validation is 28.5 m/s, corresponding to the advanced ratio of 0.15.

Fig.8 shows the wake structure for the scaled model rotor. The tip vortex and roll-up vortex in both the advancing and the retreating sides are captured. Fig.9 and Fig.10 show the inflow velocities in longitudinal and lateral directions, respectively. Compared to the results from the free wake method[44], the inflow velocities from the vortex method have better consistency with the experimental results. This is because the precision of the free wake method depends on some empirical parameters, such as the tip vortex roll-up model and vortex core model, while VVPM does not. Besides, the calculation results presented are in reasonable arrangement with those from Ref.[33], where the treecode accelerated the panel/VVPM hybrid model of a helicopter rotor. The results indicate the efficacy and practicability of the computational method in this paper.

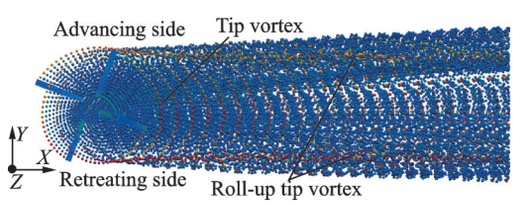

Fig.8 Wake structure for the scaled model rotor at advanced ratio of 0.15

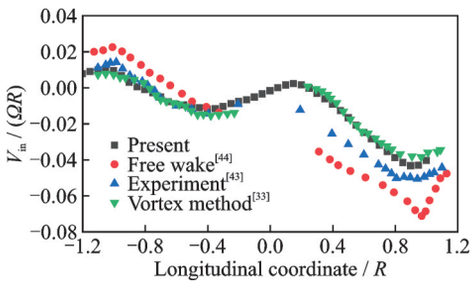

Fig.9 Inflow velocities in longitudinal direction

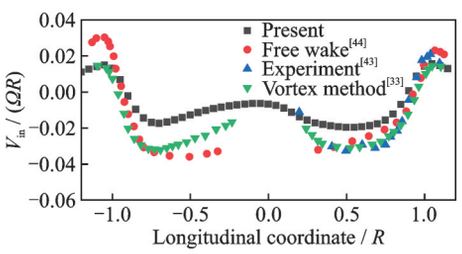

Fig.10 Inflow velocities in lateral direction

3.3 Tandem rotors

The study involves the prediction and comparison of thrusts and power requirements for the tandem-rotors configuration in both hover and level forward flight states with experimental data[45]. The tandem-rotors configuration consists of two two-blade rotors positioned horizontally with a 4.724 m offset between them. For each rotor, the blades with NACA0012 airfoil section are untapered and untwisted. The rotor has a radius of 2.286 m and a solidity of 0.054.

Considering the symmetry arrangement of tandem rotors in hover, only the performance of the front rotor is shown in Fig.11. As we can see, when the power coefficient C_P is greater than 0.015, the average relative error between the experimental and calculated thrust coefficients is less than 10%. Although there exists a slightly larger error when C_T and C_P are small, the computed and experimental results demonstrate consistent overall trends, indicat-

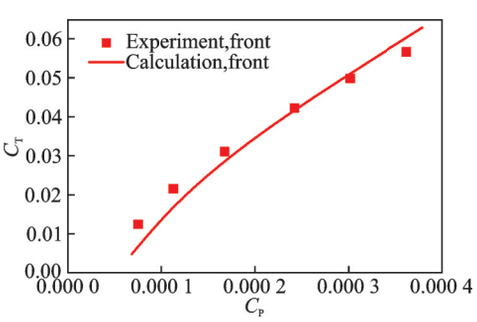

Fig.11 Hover performance of tandem-rotors

ing good agreement between them.

Fig.12 shows the power requirement variations with the change of advance ratio when the thrust coefficient C_T is fixed as 0.003 4. It can be found that the power requirement of the rear rotor is always larger than that of the front rotor, which means there is a serious downwash interference acting on the rear rotor from the front rotor. Moreover, compared with the experimental results, a slightly larger error occurs for the power requirement of the front rotor and the total power requirement when the advance ratio is larger than 0.2, while the overall trend is consistent. This may be because the general Mach number correction model for lift coefficient calculation we adopted overpredicted the lift with the Mach number increasing. Consequently, the computational results exhibit a higher lift-to-drag ratio at high flight speeds compared to the experimental results, which manifests as a lower power coefficient in the trimming state of the high advance ratio.

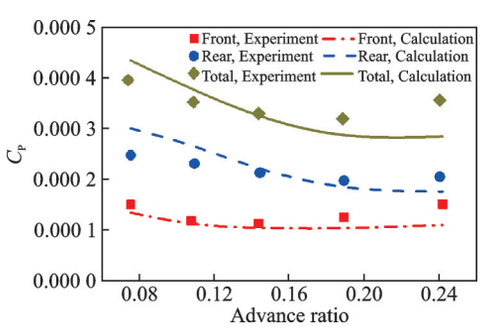

Fig.12 Level-flight performance at C_T=0.003 4

4 Results and Discussion

4.1 Numerical conditions

The numerical simulations of the multi-lift system are based on the steady flight states obtained by the hybrid hierarchical optimization trimming method. As shown in Fig.3, the helicopters are in a symmetrical arrangement with equal load distribution. The trimming results of Heli 3 and Heli 4 are the same in the longitudinal direction, as do the results of Heli 1 and Heli 2. Table 2 shows the trimming results of Heli 1 and Heli 4 at different flight speeds, where $\theta_{0,F}$ and $\theta_{0,R}$ are the collective pitch angles of the front and rear rotors respectively, θ is the pitch angle, $A_{1,F}$ and $A_{1,R}$ are the lateral cyclic pitch angles, $a_{0,F}$ and $a_{0,R}$ are the constant items of flapping angles in Fourier series, and $a_{1,F}$ and $a_{1,R}$ are the cosine items of flapping angles in Fourier series. It is worth mentioning that the longitudinal movement of the tandem helicopter is entirely achieved by adjusting the collective pitch angles of the front and rear rotors in opposite directions, so the longitudinal cyclic pitch angles are equal to zeros. Moreover, the roll angles of Heli 1 and Heli 4 are about −4° while those of Heli 2 and Heli 3 are 4°. The positions of Heli 1, Heli 2, Heli 3, Heli 4 and the "load" in earth axis are [−1.8, −1.8, −3.7], [−1.8, 1.8, −3.7], [1.8, 1.8, −3.7], [1.8, −1.8, −3.7] and [0, 0, 0], respectively.

It should be noted that it is essential and necessary to get the steady-flight states before interference exploration. Without trimming, arbitrarily given attitudes of helicopters or manipulations of the rotors cannot reflect the actual flight status of the multi-lift system, and related results of interference or performance will be meaningless. Trimming results in Table 2 provides initial system states required in vortex method, ensuring the reliability of the interference simulation and performance calcula-

Table 2 Trimming results of Heli 1 and Heli 4

Advance ratio	0		0.04		0.06		0.08		0.1		0.14	
	Heli 1	Heli 4	Heli 1	Heli 4	Heli 1	Heli 4	Heli 1	Heli 4	Heli 1	Heli 4	Heli 1	Heli 4
$\theta_{0,F}$/(°)	5.5	5.7	4.0	5.0	3.7	4.8	4.2	4.6	4.1	4.6	4.6	5.2
$A_{1,F}$/(°)	0.0	0.0	0.4	0.8	0.9	1.2	0.7	1.4	0.9	1.2	1.0	1.0
$a_{0,F}$/(°)	1.7	1.8	1.4	1.7	1.5	1.7	1.8	1.6	1.8	1.6	1.8	1.5
$a_{1,F}$/(°)	0.0	0.0	0.6	1.0	1.2	1.5	1.2	1.7	1.5	1.7	1.9	1.9
$\theta_{0,R}$/(°)	5.6	5.8	4.5	5.3	4.4	5.7	4.7	5.8	4.9	5.7	5.4	6.1
$A_{1,R}$/(°)	0.0	0.0	0.4	0.7	0.8	1.1	0.7	1.2	0.7	1.1	0.7	0.9
$a_{0,R}$/(°)	1.7	1.8	1.7	1.8	1.8	2.1	2.0	2.1	2.2	2.1	2.2	2.0
$a_{1,R}$/(°)	0.0	0.0	0.7	1.0	1.2	1.5	1.3	1.8	1.6	1.8	2.1	2.1
θ(°)	3.4	−3.9	2.8	−5.3	1.8	−7.2	0.5	−7.7	−0.8	−8.9	−4.3	−11.4

tion in the following.

4.2 Interferences at different flight speeds

Based on the trimming results above, several steady-flight states are calculated first to explore the aerodynamic interferences. For example, Fig.13 and Fig.14 show the wake structures during hovering and at an advance ratio of 0.1 after ten rotor revolutions, respectively. As we can see, there is almost no interaction between the four tandem helicopters while hovering. Furthermore, the interference becomes serious at the advance ratio of 0.1, particularly for the helicopters in the front-and-rear arrangement. Besides, it can be found that the slung load is not immersed in the rotor wake from helicopters, whether in hovering or forward flight, indicating no downwash interference acting on the load. Furthermore, from the trimming results in Table 2 and wake structures in Fig.13 and Fig.14, trimming states and interference influences of Heli 1 and Heli 2 are the same, and similar results can be concluded for Heli 3 and Heli 4. Therefore, Heli 1 and Heli 4 are taken as examples for the following discussion.

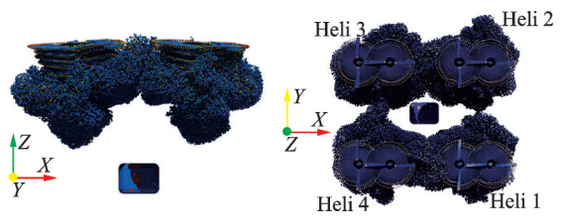

Fig.13 Wake structure in hovering

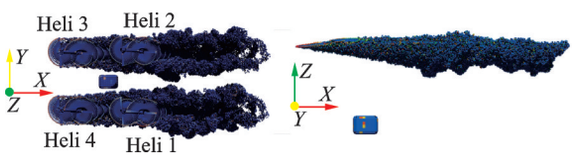

Fig.14 Wake structure at advance ratio of 0.1

Fig.15 shows sectional velocity fields at different flight speeds for Heli 1 and Heli 4. While hovering, shown in Figs.15(a,b), large down-wash velocities exist in the area from the rotor disk to two rotor diameters below the disk. The upward velocity is caused by wake diffusion and roll-up. At (0 m, 0 m, 3 m), the upward velocity is twice that at (±3.8 m, 0, 2 m) due to the wake coincidence of Heli 1 and Heli 4. The wake inclination is related to the attitudes towards helicopters. The pitch angles of Heli 1 and Heli 4 while hovering are 3.4° and −3.9°, respectively. So, in Fig.15(b), the wake of Heli 4 tilts left and the one of Heli 1 tilts right.

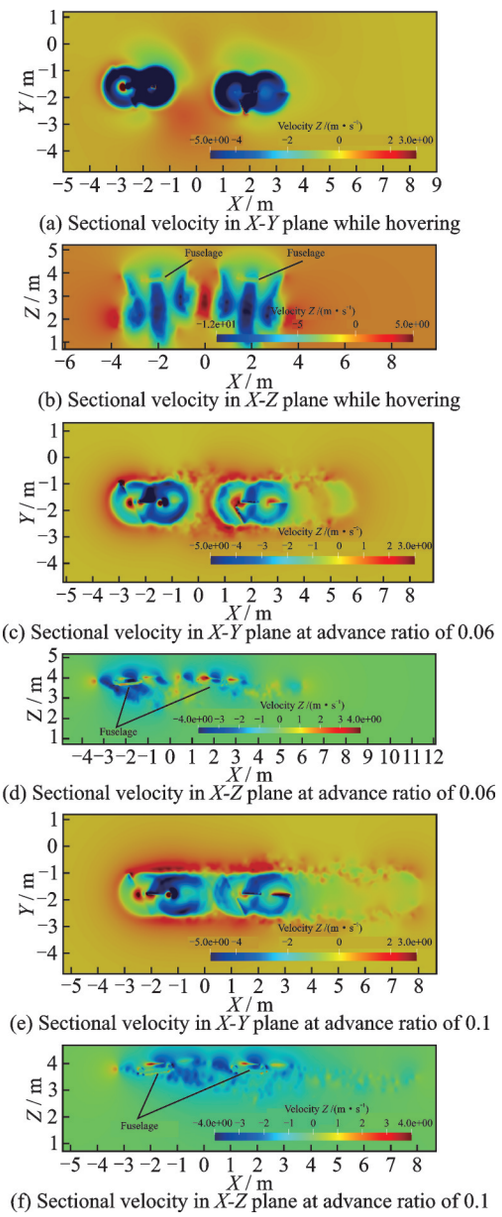

Fig.15 Sectional velocity fields of Heli 1(right) and Heli 4(left) at different flight speeds

At the advance ratio of 0.06 shown in Figs.15(c,d), the wake tilts towards the direction of incoming flow, bringing velocities upward from the roll-up tip vortex of Heli 4 to the front rotor of Heli 1. Although this is beneficial to increase the attack angle of the front rotor of Heli 1, the roll-up tip vortex resulting in unsteady aerodynamic force will cause a more complex working environment of the rotor.

Moreover, at the advance ratio of 0.1, more and more down-wash velocities generated by Heli 4 act on the rotor blade of Heli 1. Compared to the advance ratio of 0.06, the thrust of Heli 1 reduces by 3.6%, and power consumption increases by 2.3%.

In conclusion, there is almost no aerodynamic interference while hovering for the baseline configuration of four tandem helicopters carrying a load cooperatively. With the increased flight speed, the interference becomes more and more serious, especially between the helicopters in the front-rear arrangement. Besides, it can be found that interference is complex and will bring different effects on performance at different flight speeds. For seeking ways to improve performance and reduce interference meanwhile, the following sections focus on exploring the interference variations and related influence factors.

In the following discussion, Heli 1 and Heli 4 are taken as examples. The definitions of rotational directions of the front and rear rotors and longitudinal and lateral relative distances between Heli 1 and Heli 4 are shown in Fig.16. And to reduce the number of variables, the advance ratio in simulations is fixed as 0.1, which corresponds the worst case relatively.

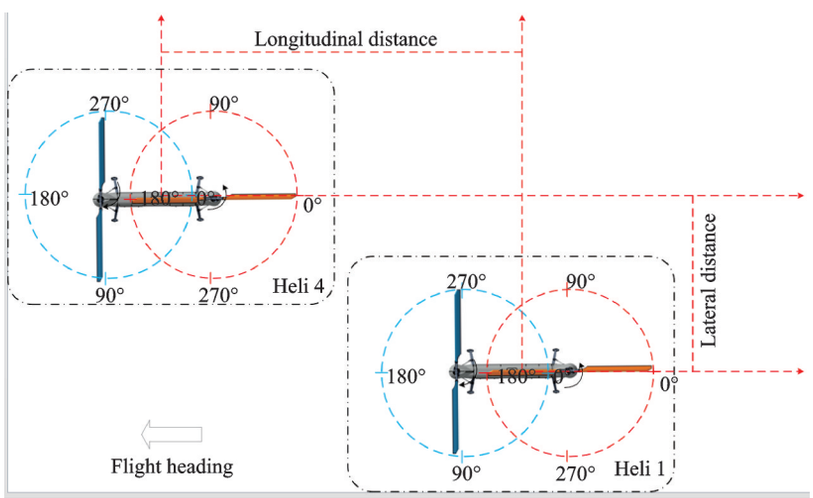

Fig.16 Arrangements of Heli 1(right) and Heli 4(left)

Besides, we assume that in the following discussions, the differences of lateral, longitudinal and height relative positions have little effect on the trimming state. So, the trimming variables are fixed as those in Table 2.

And in the following figures, 100% thrust of the front rotor corresponds to 95 N and that of the rear rotor to 83 N. Meanwhile, 100% power of the front rotor corresponds to 310 W and that of the rear rotor to 452 W. These values of Heli 1 are obtained by the calculation results when Heli 4 is excluded.

4.3 Interferences and performances at different lateral relative positions

This section shows the aerodynamic interferences with changes in lateral relative positions from $-1.5D$ to $1.5D$, where D represents the rotor diameter, $-1.5D$ represents the arrangement in which Heli 1 is located at the lateral position of negative 1.5 rotor diameters relative to that of baseline configuration, and $1.5D$ represents the arrangement in which Heli 1 is located at the lateral position of positive 1.5 rotor diameters relative to that of baseline configuration.

In Fig.17, the sectional vorticity fields in X-Y plane with three typical relative positions are depicted. For the baseline configuration, the tandem rotors of Heli 1 are completely immersed in the rotor wake of Heli 4. For the arrangement in which Heli 1 move 0.9 m to the left ($-0.5D$), only the portion of the front rotor's retreating side and the rear rotor's advancing side of Heli 1 are situated within the rotor wake of Heli 4. With the increase of lateral displacement as shown in Fig.17(c), there is almost no in-

terference between Heli 1 and Heli 4. Besides, it is worth mentioning that results of rightward displacement are similar to those of leftward displacement except that the advancing side of the front rotor and retreating side of the rear rotor of Heli 1 are immersed in the rotor wake from 0.5D to 1.0D appropriately.

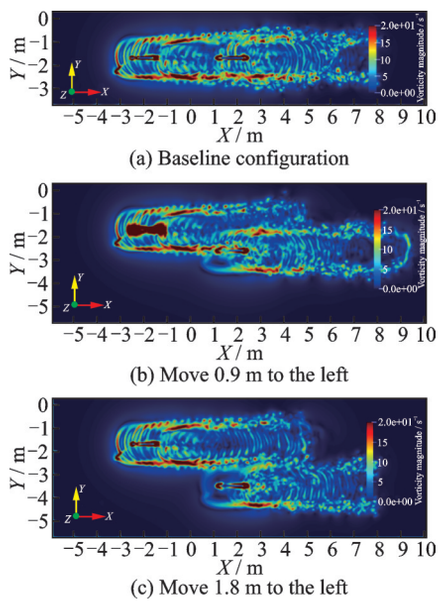

Fig.17 Sectional vorticity fields of Heli 1(right) and Heli 4 (left) with different lateral relative positions

Fig.18 shows the sectional force at 0.75R of the front rotor for Heli 1. As we can see, there exist big differences between the three cases for azimuth angles from 100° to 250°. In the baseline configuration, Heli 1 is entirely immersed in the rotor wake of Heli 4, so the sectional force at 0.75R is much smaller than the other two. For Case "Left 0.9 m", the sectional forces with azimuth angles from 200° to 250° are dropped significantly compared with those from 100° to 170°. Meanwhile, for Case "Left 1.8 m", the sectional forces always have large values. Those results are consistent with the interference variations with different lateral relative positions mentioned above. According to sectional forces at 0.75R of the rear rotor shown in Fig.19, we can see that relative positions have little effect on the thrust distribution. This is due to the fact that the front rotor causes significantly more interference to the rear rotor than Heli 4 does.

Fig. 20 and Fig.21 show the thrust and power

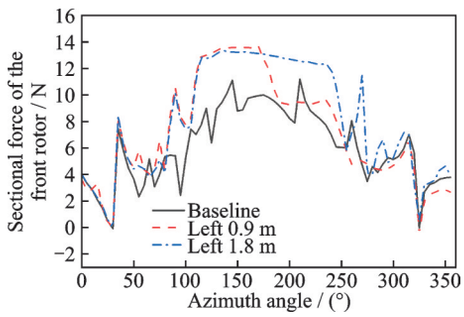

Fig.18 Sectional force at 0.75R of the front rotor with different lateral relative positions of Heli 1

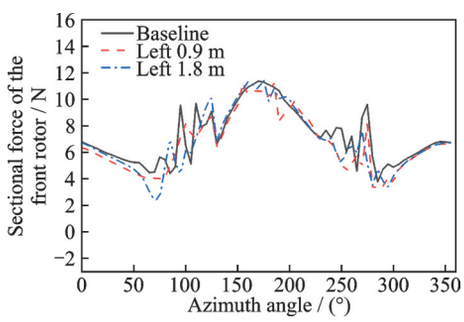

Fig.19 Sectional force at 0.75R of the rear rotor with different lateral relative positions of Heli 1

variations of Heli 1 with the change of lateral relative positions, respectively. For the baseline configuration in which lateral relative position equals to 0, there exist 20% thrust loss and 15% power increase for the front rotor. With the increase of lateral relative position positively or negatively the thrust increases and the power decreases. Within ranges from −1.5D to −0.75D and from 0.75D to 1.5D, the thrust values are larger and powers are smaller than those of the case without interference, which benefits from the increased attack angles due to little downwash interference and roll-up tip vortex. Besides, for the rear rotor, the changes of thrust and power are little. This is consistent with the results of the sectional force.

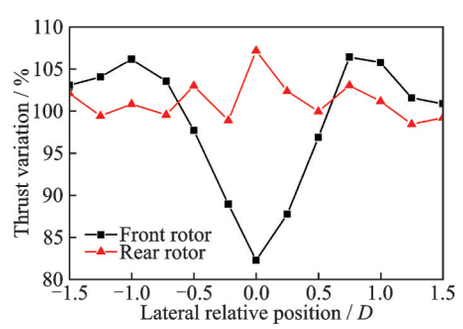

Fig.20 Thrust variation with the change of lateral relative position

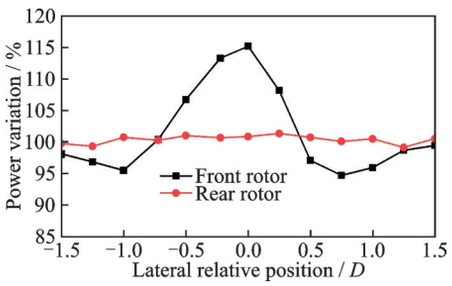

Fig.21 Power variation with the change of lateral relative position

In summary, there exist larger thrust loss and higher power consumption for Heli 1 in the baseline configuration. The thrust loss and power consumption will be reduced by adjusting the relative lateral distance between Heli 1 and Heli 4 appropriately. Furthermore, within lateral distance ranges from $-1.5D$ to $-0.75D$ and from $0.75D$ to $1.5D$, the performance is even better than that of the case without interference.

4.4 Interferences and performances at different longitudinal relative position

Calculation of aerodynamic interference with the change of longitudinal relative position is demonstrated in this section. Fig.22 shows the sectional vorticity fields when Heli 1 is located at forward and backward 0.9 m relative to the baseline configuration respectively. Compared to the vorticity field of baseline configuration shown in Fig.17(a), we can infer that the closer the longitudinal distance between Heli 1 and Heli 4, the greater the aerodynamic interference.

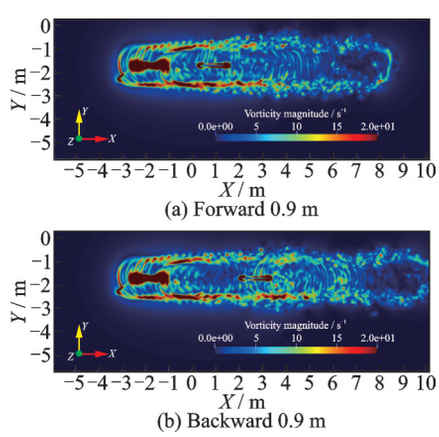

Fig.22 Sectional vorticity fields of Heli 1(right) and Heli 4 (left) with different longitudinal relative positions

Fig.23 and Fig.24 show the sectional force at $0.75R$ of the front and rear rotors with different longitudinal relative positions, respectively. As shown in Fig.23, in most areas sectional forces at $0.75R$ of Case "Backward 0.9 m" are larger than those of the other two cases. This agrees with the change of aerodynamic interference mentioned above. Similar to the calculation results with different lateral relative positions, the sectional force change of the rear rotor is little. This fact also results in small changes of resultant thrust and power as shown in Fig.25 and Fig.26, respectively.

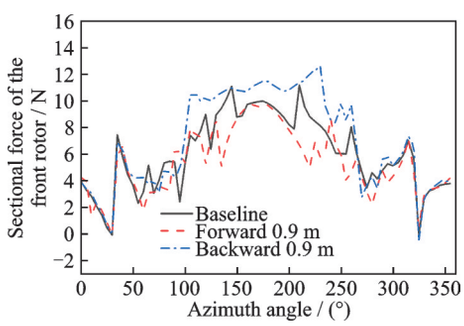

Fig.23 Sectional force at $0.75R$ of the front rotor with different longitudinal relative positions of Heli 1

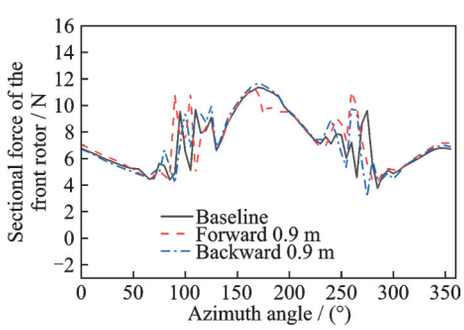

Fig.24 Sectional force at $0.75R$ of the rear rotor with different longitudinal relative positions of Heli 1

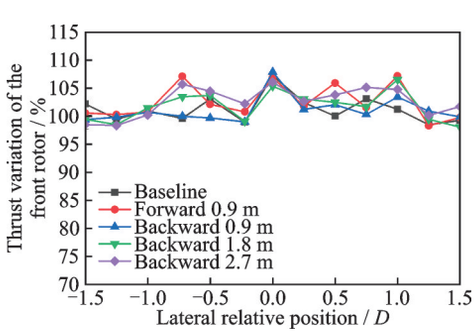

Fig.25 Thrust variation of the rear rotor with different longitudinal relative positions

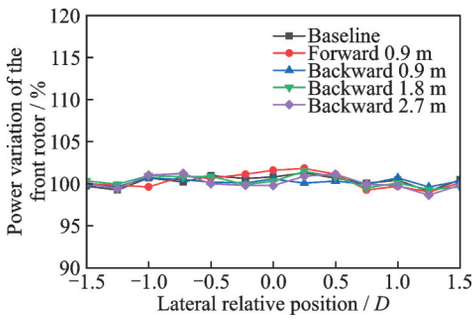

Fig.26 Power variation of the rear rotor with different longitudinal relative positions

Fig.27 and Fig.28 show the resultant thrust and power of the front rotor with different longitudinal relative positions, respectively. As we can see, when the lateral relative position is between $-0.5D$ to $0.5D$, the thrust reduction and power consumption decrease as the longitudinal distance between Heli 1 and Heli 4 increases. Moreover, when the lateral relative position is between $-1.5D$ to $-0.5D$ or $0.5D$ to $1.5D$, the thrust reduction and power consumption increase as the longitudinal distance increases. This is because that the smaller the longitudinal distance, the more roll-up vortex resulted upwash velocity acting on the blade element.

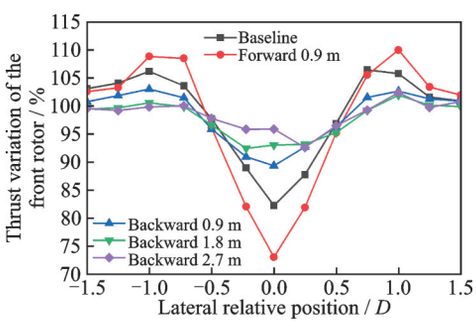

Fig.27 Thrust variation of the front rotor with different longitudinal relative positions

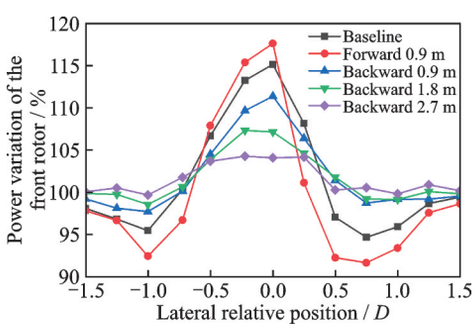

Fig.28 Power variation of the front rotor with different longitudinal relative positions

4.5 Interferences and performances at different relative heights

The sectional vorticity fields in X-Z plane with three typical relative heights are shown in Fig.29. It can be seen that in the baseline configuration, the font part of Heli 1 is immersed in the rotor wake from Heli 4. For the arrangement in which Heli 1 is 0.7 m up relative to that of the baseline configuration, there is almost no aerodynamic interference between Heli 1 and Heli 4. When Heli 1 is 0.7 m down, Heli 1 is almost entirely immersed in the wake vortex of Heli 4.

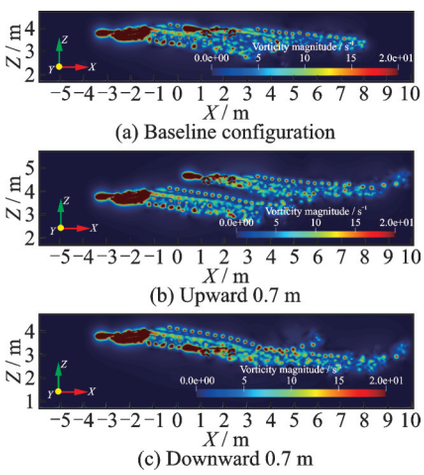

Fig.29 Sectional vorticity fields with different relative heights

Sectional forces at $0.75R$ of the front and rear rotors with different relative heights are shown in Fig.30 and Fig.31, respectively. When Heli 1 is 0.7 m up, the sectional forces of the front rotor with azimuth angle ranges from 100° to 250° are larger and have smaller fluctuation relative to the other two. For the rear rotor when Heli 1 is 0.7 m down, the sectional forces are smaller in most areas be-

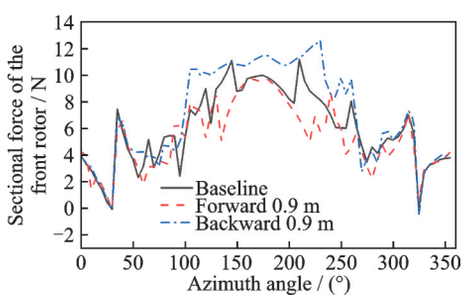

Fig.30 Sectional force at $0.75R$ of the front rotor with different relative heights of Heli 1

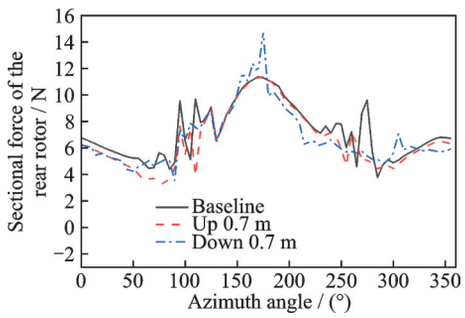

Fig.31 Sectional force at 0.75R of the rear rotor with different relative heights of Heli 1

cause Heli 1 is entirely immersed in the rotor wake.

Fig.32 and Fig.33 show the resultant thrust and power of the front rotor with different relative heights respectively. For the baseline configuration and the case when Heli 1 is 0.7 m down, there exist about 20% thrust reduction and 15% power addition while the lateral relative position is 0. With the increase of lateral distance between Heli 1 and Heli 4 no matter positively or negatively, the thrust increases and the power decreases. For the cases when Heli 1 is 0.7 m up, 1.4 m up and 0.7 m down, the thrust and power are close to those without interference. Fig.34 and Fig.35 show the resultant thrust and power of the rear rotor with different relative

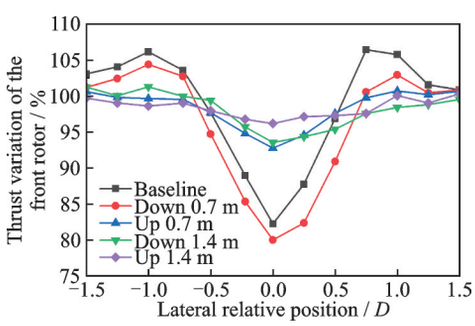

Fig.32 Thrust variation of the front rotor with different relative heights

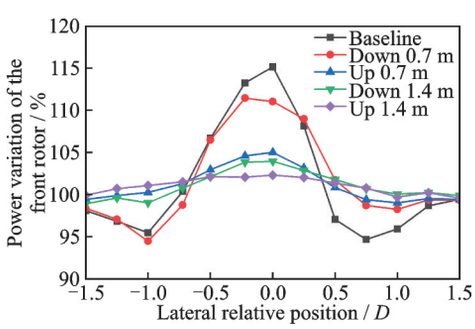

Fig.33 Power variation of the front rotor with different relative heights

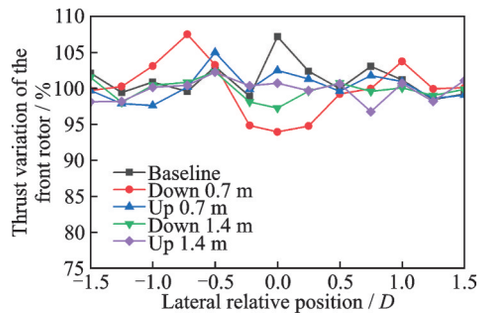

Fig.34 Thrust variation of the rear rotor with different relative heights

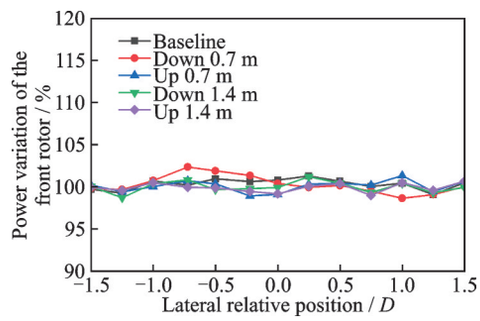

Fig.35 Power variation of the rear rotor with different relative heights

heights, respectively. In all cases, the thrust and power variations are relatively small.

4.6 Formation recommendation

Based on the explorations above, at advance ratio of 0.1, the latera relative distances from $-1.5D$ to $-0.75D$ and $0.75D$ to $1.5D$ are beneficial to reduce interference, thrust loss and power consumption. There is almost no interference when the longitudinal distance is larger than $3.5D$. Locating the rear helicopter $0.5D$ higher or more than the front one is favorable to improve performance. Since the interference at advance ratio of 0.1 corresponds the relatively worst case, the conclusions above are suitable for hovering and other advance ratios smaller than 0.1.

Therefore, it can be concluded that larger lateral or longitudinal distance and locating the helicopter behind at higher height are favorable from the perspective of reducing aerodynamic interference and improving performance. This means the isosceles trapezoid formation and the rectangle formation in which helicopters behind are located at higher heights or far enough in the longitudinal direction as

shown in Fig.36 and Fig.37 should be recommended. Table 3 shows the thrust addition and power reduction ratios compared to the baseline.

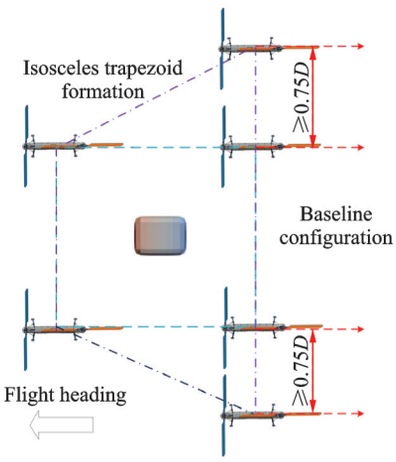

Fig.36 Isosceles trapezoid formation

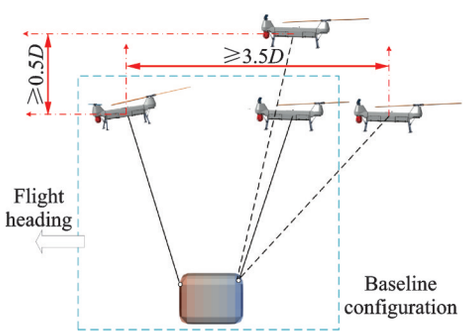

Fig.37 Rectangle formation

Table 3 Thrust addition and power reduction ratios compared to the baseline

0.75*D* lateral		3.5*D* longitudinal		0.5*D* height	
Thrust	Power	Thrust	Power	Thrust	Power
7.9% ↑	8.1% ↓	6.7% ↑	5.8% ↓	2.9% ↑	4.7% ↓

5 Conclusions

The aerodynamic interference and resulted performance changes of helicopters in the multi-lift system at steady flight state are investigated by the vortex approach. A baseline configuration of four tandem helicopters carrying a load cooperatively with the "2-lead" formation is introduced to explore the interferences. The vortex approach combining the lifting surface theory and viscous vortex method is validated by related wind tunnel test data. The steady flight states are calculated based on the hybrid hierarchical trimming method. On the basis, several numerical simulations are developed and the following conclusions are obtained:

(1) There indeed exists serious interference between helicopters in front-and-rear arrangement at forward flight state. The interference is complex and resulted effects on performance are different at different advance ratios.

(2) At the advance ratio of 0.1, for the baseline configuration there exist a 20% thrust loss and 15% power increase for the front rotor of the tandem helicopter behind.

(3) At the advance ratio of 0.1, the lateral relative distances from $-1.5D$ to $-0.75D$ and $0.75D$ to $1.5D$ are beneficial to reduce interference, thrust loss and power consumption. There is almost no interference when the longitudinal distance is larger than $3.5D$. Locating the rear helicopter higher than the front one is favorable to improve performance.

(4) The isosceles trapezoid formation and the rectangle formation in which rear helicopters are located at higher heights or far enough in the longitudinal direction are recommended to reduce interference and improve performance.

Reference

[1] LEWIS J, MARTIN C. Models and analysis for twin-lift helicopter systems[C]//Proceedings of 1983 American Control Conference. Piscataway, NJ: IEEE, 1983: 1324-1325.

[2] MITTAL M, PRASAD J V R, SCHRAGE D P. Comparison of stability and control characteristics of two twin-lift helicopter configurations[J]. Nonlinear Dynamics, 1992, 3(3): 199-223.

[3] BERNARD M. A system of autonomously flying helicopters for load transportation[D]. Ilmenau: TU Ilmenau, 2013.

[4] SHERIDAN P F. Feasibility study for multiple helicopter heavy lift systems: Vertol Report R-136 [R]. Philadelphia, PA: Vertol Aircraft Corporation, 1957.

[5] MEEK T, CHESLEY G B. Twin helicopter lift system study and feasibility: SER-64323[R]. Stratford, Conn: Sikorsky Aircraft Corporation, 1970.

[6] BERNARD M, KONDAK K. Generic slung load transportation system using small size helicop-

ters[C]//Proceedings of 2009 IEEE International Conference on Robotics and Automation. Piscataway, NJ: IEEE, 2009: 3258-3264.

[7] BISGAARD M, BENDTSEN J D, LA COUR-HARBO A. Modeling of generic slung load system[J]. Journal of Guidance, Control, and Dynamics, 2009, 32(2): 573-585.

[8] RAZ R, FOGEL O, ROSEN A, et al. Using wind tunnel tests to investigate dual lift trim, maneuvers, stability and control[C]//Proceedings of the AHS International 73rd Annual Forum & Technology Display. Phoenix, AZ: AHS, 2017: 2744-2760.

[9] CURTISS H C. Studies of the dynamics of the twin-lift system: MAE TR No.1840[R]. Princeton, NJ: Princeton University,1988.

[10] PRASAD J V R, MITTAL M, SCHRAGE D P. Control of a twin lift helicopter system using nonlinear state feedback[J]. Journal of the American Helicopter Society, 1991, 36(4): 57-65.

[11] MITTAL M, PRASAD J. Input-output linearization of a three dimensional model of a twin-lift helicopter system[C]//Proceedings of Navigation and Control Conference. Reston, VA: AIAA, 1993: 2754.

[12] CICOLANI L S. Equations of motion of slung-load systems, including multilift systems[M]. Washington, D C: NASA, 1992.

[13] RAZ R, ROSEN A. Trim and stability of a twin-lift system in forward flight[J]. Journal of the American Helicopter Society, 2005, 50(2): 138-149.

[14] CARTER E S. Implication of heavy lift helicopter size effect trends and multilift options for filling the need[C]//Proceedings of Association Aeronautique et Astronautique de France, European Rotorcraft Forum. Aix-en-Provence, France:[s.n.], 1982.

[15] LI Z Q, HORN J F, LANGELAAN J W. Coordinated transport of a slung load by a team of autonomous rotorcraft[C]//Proceedings of AIAA Guidance, Navigation, and Control Conference. Reston, VA: AIAA, 2014: 0968.

[16] POWELL D, CICOLANI L, BERRIOS M, et al. Stability, control, and simulation of a dual lift system using autonomous R-MAX helicopters[C]//Proceedings of the 70th American Helicopter Society Annual Forum. Montreal, Quebec, Canada: AHS, 2014: 2195-2213.

[17] ENCIU J, HORN J F, LANGELAAN J W. Formation control of a rotorcraft multilift system[J]. Journal of the American Helicopter Society, 2017, 62(4): 1-14.

[18] ENCIU J, HORN J F. Flight performance optimization of a multilift rotorcraft formation[J]. Journal of Aircraft, 2017, 54(4): 1521-1538.

[19] TAKAHASHI M, WHALLEY M, BERRIOS M G, et al. A system for autonomous rotorcraft dual-lift flight research[C]//Proceedings of the 74th Annual Forum of the American Helicopter Society. Phoenix, AZ: AHS, 2018: 1-18.

[20] GIMENEZ J, SALINAS L R, GANDOLFO D C, et al. Control for cooperative transport of a bar-shaped payload with rotorcraft UAVs including a landing stage on mobile robots[J]. International Journal of Systems Science, 2020, 51(16): 3378-3392.

[21] TAKAHASHI M D, WHALLEY M S, BERRIOS M G, et al. Flight validation of a system for autonomous rotorcraft multilift[J]. Journal of the American Helicopter Society, 2019, 64(3): 1-13.

[22] BERRIOS M, TAKAHASHI M, WHALLEY M, et al. Load distribution control and swing angle feedback for an autonomous dual lift system with flight test results[C]//Proceedings of the 74th Annual Forum of the American Helicopter Society. Phoenix, AZ: AHS, 2018.

[23] CICOLANI L S. Quasi-steady maneuvering of pendant dual lift systems: FCDDAMV-19-01[R]. San Jose: San Jose State University Research Foundation, 2019.

[24] LEISHMAN G J. Principles of helicopter aerodynamics with CD extra[M]. Cambridge: Cambridge University Press, 2006.

[25] YEMENICI O, SEZER-UZOL N, UZOL O. Investigation of rotor-rotor interactions for two helicopters in forward flight using free-vortex wake methodology[C]//Proceedings of the 28th AIAA Applied Aerodynamics Conference. Reston, VA: AIAA, 2010: 4558.

[26] DUIVENVOORDEN R, VOSKUIJL M, MORÉE L, et al. Numerical and experimental investigation into the aerodynamic benefits of rotorcraft formation flight[J]. Journal of the American Helicopter Society, 2022, 67(1): 1-17.

[27] JAIN K P, FORTMULLER T, BYUN J, et al. Modeling of aerodynamic disturbances for proximity flight of multirotors[C]//Proceedings of 2019 International Conference on Unmanned Aircraft Systems

(ICUAS). Piscataway, NJ: IEEE, 2019: 1261-1269.

[28] SHI G, HÖNIG W, YUE Y, et al. Neural-swarm: Decentralized close-proximity multirotor control using learned interactions[C]//Proceedings of 2020 IEEE International Conference on Robotics and Automation (ICRA). Piscataway, NJ: IEEE, 2020: 3241-3247.

[29] YAMAUCHI G K, WADCOCK A J, DERBY M R. Measured aerodynamic interaction of two tiltrotors[C]//Proceedings of Annual Forum Proceedings-American Helicopter Society. Phoenix, AZ: AHS, 2003, 59(2): 1720-1731.

[30] TAN J F, ZHOU T Y, SUN Y M, et al. Numerical investigation of the aerodynamic interaction between a tiltrotor and a tandem rotor during shipboard operations[J]. Aerospace Science and Technology, 2019, 87: 62-72.

[31] COTTET G H, KOUMOUTSAKOS P D. Vortex methods: Theory and practice[M]. Cambridge: Cambridge University Press, 2000.

[32] OPOKU D G, TRIANTOS D G, NITZSCHE F, et al. Rotorcraft aerodynamic and aeroacoustic modeling using vortex particle methods[C]//Proceedings of the 23rd International Congress of Aeronautical Sciences (ICAS 2002). Toronto, ON, Canada: ICAS, 2002: 8-13.

[33] TAN J, WANG H. Simulating unsteady aerodynamics of helicopter rotor with panel/viscous vortex particle method[J]. Aerospace Science and Technology, 2013, 30(1): 255-268.

[34] ALVAREZ E J, NING A. Modeling multirotor aerodynamic interactions through the vortex particle method[C]//Proceedings of AIAA Aviation 2019 Forum. Reston, VA: AIAA, 2019: 2827.

[35] MAS-GALLIC S. Deterministic particle method: Diffusion and boundary conditions[J]. Lectures in Applied Mathematics: Vortex Methods and Vortex Dynamics, 1991, 28: 433-465.

[36] LINDSAY K, KRASNY R. A particle method and adaptive treecode for vortex sheet motion in three-dimensional flow[J]. Journal of Computational Physics, 2001, 172(2): 879-907.

[37] CHENG H, GREENGARD L, ROKHLIN V. A fast adaptive multipole algorithm in three dimensions[J]. Journal of Computational Physics, 1999, 155(2): 468-498.

[38] PAKALNIS E. Lift and drag force calculation methods using non-linear section data: History and recent research[J]. Aviation, 2004, 8(2): 9-13.

[39] LEISHMAN J G, BI N. Experimental investigation of rotor/lifting surface interactions[J]. Journal of Aircraft, 1994, 31(4): 846-854.

[40] DUAN D, DING Z, ZHAO H, et al. Optimal hierarchical trimming method for multi-lift system with helicopters considering aerodynamic interference[J]. Aerospace Science and Technology, 2022, 128: 107785.

[41] CARADONNA F X, TUNG C. Experimental and analytical studies of a model helicopter rotor in hover[J]. Vertica, 1981. DOI: 10.1016/0376-0421(81)90002-6.

[42] RAJMOHAN N, ZHAO J, HE C. A coupled vortex particle/CFD methodology for studying coaxial rotor configurations[C]//Proceedings of the Fifth Decennial AHS Aeromechanics Specialists' Conference, VA USA: VFS, 2014.

[43] ALTHOFF S L, ELLIOTT J W, SAILEY R H. Inflow measurement made with a laser velocimeter on a helicopter model in forward flight. Volume 1: Rectangular planform blades at an advance ratio of 0.15: NASA-TM-100541[R]. [S.l.]: NASA, 1988.

[44] BHAGWAT M J. Mathematical modeling of the transient dynamics of helicopter rotor wakes using a time-accurate free-vortex method[D]. Maryland: University of Maryland at College Park, 2001.

[45] DINGELDEIN R C. Wind-tunnel studies of the performance of multirotor configurations[M]. Washington, DC: National Advisory Committee for Aeronautics, 1954.

Authors Dr. **DING Zhiwei** received his B.S. degree in engineering from the National Key Laboratory of Rotorcraft Aerodynamics, Nanjing University of Aeronautics and Astronautics, in 2013. In 2014, he studied for a M.S. degree at the same laboratory and switched to studying for a Ph.D degree in 2016. His primary focus is rotorcraft aerodynamic modeling and optimization design, and his research interests mainly include high-speed rotorcraft and new configuration eVTOL.

Prof. **LI Jianbo** received the B.S. and Ph.D. degrees in aerospace vehicle design from Nanjing University of Aeronautics and Astronautics (NUAA), Nanjing, China, in 2000 and 2003, respectively. From 2006 to 2008, he was an assistant professor in State Key Laboratory of Helicopter Rotor of Dynamics, NUAA and in 2009, he became a full professor. His

research has focused on aerodynamics, flight dynamics and preliminary design of traditional helicopter, wind milling rotor aircraft, ducted fan aircraft and rotor/wing compound aircraft.

Author contributions Dr. **DING Zhiwei** wrote the core code of arodynamics and conducted related analysis. Dr. **DUAN Dengyan** contributed to model components and data analysis. Mr. **ZHAO Gang** and Ms. **XUAN Jinting** contributed to the discussion and background of the study. Prof. **LI Jianbo** proposed the problem and provided technical support. All authors commented on the manuscript draft and approved the submission.

Competing interests The authors declare no competing Interests.

(Production Editor: SUN Jing)

"2-lead"多直升机升力系统的气动干扰和性能变化

丁志伟，段登燕，赵 刚，宣金婷，李建波

(南京航空航天大学航空学院直升机动力学全国重点实验室，南京 210016，中国)

摘要：参与协同吊挂的直升机属于近距离编队飞行，旋翼尾流之间存在严重的气动干扰，从而带来复杂的气动力学耦合问题。因此在研究性能优化、先进编队控制之前，有必要研究协同吊挂系统的气动干扰及其带来的性能变化。本文以4架纵列式直升机组成的"2-lead"队形的协同吊挂系统为研究对象，采用黏性涡粒子/面元法研究直升机协同吊挂系统稳定飞行状态下的性能和流场。其中，系统的稳定飞行状态通过分层配平法得到，涡/面法通过风洞试验数据验证。在此基础上，研究了不同飞行速度及不同直升机相对位置下的系统气动干扰和性能变化。计算结果表明：前飞时，研究对象中前后布置的直升机间存在严重的气动干扰。其中，前进比为0.1时，队列中后方纵列式直升机的前旋翼存在20%的推力损失和15%的功耗增加。当队列中直升机间的纵向距离大于3.5倍旋翼直径D、侧向距离大于0.75倍旋翼直径D，或垂向距离大于0.5倍旋翼直径D时，气动干扰均会大大降低。

关键词：多升力；直升机；性能变化；气动干扰；涡方法；编队